ORIGINAL PAPER

AFM study of morphological changes associated with electrochemical solid–solid transformation of three-dimensional crystals of TCNQ to metal derivatives (metal=Cu, Co, Ni; TCNQ=tetracyanoquinodimethane)

Xiaohu Qu · Ayman Nafady · Adam Mechler · Jie Zhang · Alexander R. Harris · Anthony P. O'Mullane · Lisandra L. Martin · Alan M. Bond

Abstract In situ atomic force microscopy (AFM) allows images from the upper face and sides of TCNQ crystals to be monitored during the course of the electrochemical solid–solid state conversion of 50×50 μm^2 three-dimensional drop cast crystals of TCNQ to CuTCNQ or M [TCNQ]$_2$(H$_2$O)$_2$ (M=Co, Ni). Ex situ images obtained by scanning electron microscopy (SEM) also allow the bottom face of the TCNQ crystals, in contact with the indium tin oxide or gold electrode surface and aqueous metal electrolyte solution, to be examined. Results show that by carefully controlling the reaction conditions, nearly mono-dispersed, rod-like phase I CuTCNQ or M[TCNQ]$_2$(H$_2$O)$_2$ can be achieved on all faces. However, CuTCNQ has two different phases, and the transformation of rod-like phase 1 to rhombic-like phase 2 achieved under conditions of cyclic voltammetry was monitored in situ by AFM. The similarity of in situ AFM results with ex situ SEM studies accomplished previously implies that the morphology of the samples remains unchanged when the solvent environment is removed. In the process of crystal transformation, the triple phase solid|electrode|electrolyte junction is confirmed to be the initial nucleation site. Raman spectra and AFM images suggest that 100% interconversion is not always achieved, even after extended electrolysis of large 50×50 μm^2 TCNQ crystals.
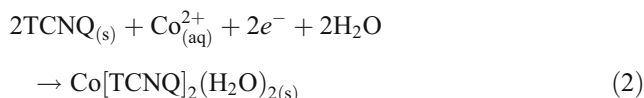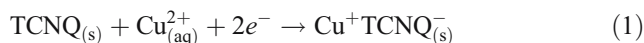
X. Qu · A. Nafady · A. Mechler · J. Zhang · A. R. Harris ·
A. P. O'Mullane · L. L. Martin · A. M. Bond (✉)
School of Chemistry, Monash University,
P.O. Box 23, Clayton, Victoria 3800, Australia
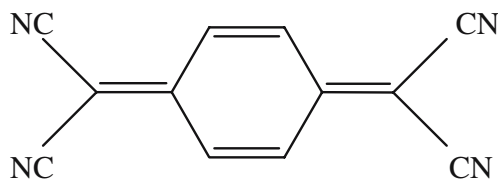e-mail: Alan.Bond@sci.monash.edu.au

Introduction

7,7,8,8-Tetracyanoquinodimethane (TCNQ; Scheme 1) has been intensively studied due to its rich array of electrical, electrochemical, optical, and spectroscopic properties [1–13].

M^{x+}[TCNQ]$_x^-$ derivatives (designated below as MTCNQ, M=transition metal) also have been synthesized and characterized. Frequently, these metal complexes behave as organic semiconductors, some of which may be used as memory storage devices or for on/off switching [14–20], as in the case with CuTCNQ [21, 22].
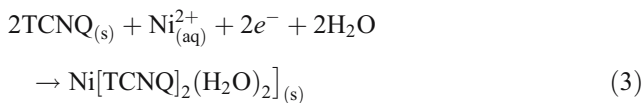
Various methods have been developed to acquire MTCNQ crystals. Our laboratory has been interested in electrochemical forms of synthesis [9, 13, 15–17, 19, 23–25] where the resulting morphology can be controlled by careful selection of electrochemical parameters. When M=Cu, Co, Ni, the solid–solid TCNQ→MTCNQ transformation that takes place at a TCNQ-modified electrode in contact with aqueous solutions of M^{x+} is based on a nucleation growth mechanism. The overall processes are respectively:

$$TCNQ_{(s)} + Cu^{2+}_{(aq)} + 2e^- \rightarrow Cu^+TCNQ^-_{(s)} \qquad (1)$$

$$2TCNQ_{(s)} + Co^{2+}_{(aq)} + 2e^- + 2H_2O$$
$$\rightarrow Co[TCNQ]_2(H_2O)_{2(s)} \qquad (2)$$

Scheme 1 7,7,8,8-Tetracyanoquinodimethane, $C_{12}H_4N_4$

$$2TCNQ_{(s)} + Ni^{2+}_{(aq)} + 2e^- + 2H_2O$$

$$\rightarrow Ni[TCNQ]_2(H_2O)_2]_{(s)} \qquad (3)$$

The mechanistic details differ with the metal ions. However, the principle electron transfer step $TCNQ_{(s)} + e^- \rightarrow TCNQ^-_{(s)}$ is dominant so that the basic features of the current potential curves observed under conditions of cyclic voltammetry or with other voltammetric protocols are not strongly metal ion dependent. On the basis of ex situ SEM observations [24, 25], it may be concluded that the topographies of the MTCNQ solids formed from reduction of TCNQ at an electrode surface also are similar. Thus, all electrochemically generated MTCNQ complexes appear to exhibit rod or needle-shaped structures, although their size is metal ion dependent, with CuTCNQ and $Co[TCNQ]_2(H_2O)_2$ crystals being significantly longer than $Ni[TCNQ]_2(H_2O)_2$ crystals.

A problem with the ex situ SEM method is that the steps of removal of the sample from the solvent and drying that are required before obtaining images may contribute to changes in the crystal morphology. Thus, in situ monitoring is needed to ensure the fidelity of conclusions related to structures formed by solid–solid transformation on a TCNQ modified electrode surface. We therefore now have introduced in situ AFM imaging to monitor the morphology changes associated with the TCNQ/MTCNQ transformation at an electrode surface. Notably, previous work has utilized AFM and scanning tunneling microscopy to characterize the morphology of groups I and II metal TCNQ-based materials [26–30]. In the present case, the in situ AFM method is applied to monitoring the changes at the top face and sides of large, three-dimensional TCNQ crystals when a potential is applied to a TCNQ modified electrode in contact with a transitional metal ion. To obtain a complete picture of the solid–solid state conversion, we also have examined ex situ, by SEM imaging, the bottom face of crystals that are adhered to the electrode surface.

Experimental section

Chemicals Analytical grade copper(II) sulfate pentahydrate, cobalt(II) nitrate hexahydrate, cobalt(II) chloride hexahydrate, nickel(II) chloride hexahydrate, 7,7′,8,8′-tetracyanoquinodi-

methane (TCNQ), 2-propanol, and acetone were used as received from Aldrich or Fluka. All aqueous solutions were prepared from water (resistivity of 18.2 $M\Omega$ cm) that had been purified by a Sartorius Arium 611 system. Indium tin oxide (ITO) glass (from Prazisions Glas and Optik GmbH) and gold-coated glass slides (from Arrandee) with a typical area of 0.20 cm^2 were used as substrates. Before use, ITO glass was cleaned by ultra-sonication for 5 min in, first, acetone and then in 2-propanol. TCNQ crystals used for both AFM and SEM electrochemical studies were prepared by drop casting 20 μL of saturated TCNQ acetonitrile solution onto the substrate and allowing the solvent to evaporate from this surface at room temperature (23±2 °C). Under these conditions, many yellow-colored rhombus-like micron-sized TCNQ crystals are formed on the substrate as observed by optical microscopy (Olympus BX51M). The TCNQ modified substrate was then assembled into an electrochemical cell and served as the working electrode. During electrochemical solid–solid transformation, the rhombus-like TCNQ crystals changed in color, from yellow to dark blue. Use of an optical microscope integrated with the AFM instrument allowed regions on the surface where crystals are present to be readily located. ITO is transparent in the visible region of the spectrum, so it is easier to locate these dark blue crystals on the surface. For this reason, optically transparent ITO is preferred to gold as a substrate in this study. However, as electrochemical data, AFM images and Raman spectra were always found to be similar on gold and ITO substrates; no significant electrode material dependence was found.

AFM images were obtained in the tapping mode using a NT-MDT Ntegra AFM instrument (NT-MDT, Russia). AFM tips were of the NC36 type (without aluminum coating) and were obtained from MikroMasch, Estonia. An Autolab μ20 potentiostat (Eco Chemie, Netherlands) was used for electrochemical control. The electrochemical cell used in the in situ AFM imaging experiments was designed by NT-MDT instruments and included a built-in platinum wire counter electrode and a solid state Ag/AgCl reference electrode, whose potential is directly related to the chloride (or sulfate, nitrate) concentration in the metal salt electrolyte solution present in the electrochemical cell. The scanning electron microscope (SEM) imager was a Philips XL30 field emission gun scanning electron microscope (FEGSEM) used with an accelerating voltage of 2 keV. Raman spectra were acquired with a Renishaw Raman RM2000 instrument using a laser strength 18 mW at a wavelength of 780 nm. All experiments were accomplished at room temperature of 23±2 °C.

Results and discussion

It is well established [31] that application of a sufficiently negative potential can induce the conversion of TCNQ,

adhered on an electrode surface, to MTCNQ, in the presence of $M_{(aq)}^{x+}$. When the chemically modified electrode is in contact with the relevant metal salt solutions [16, 24, 25, 32] (M=Cu^{2+}, Co^{2+}, Ni^{2+}), electrochemically induced transformation of TCNQ to $Co[TCNQ]_2(H_2O)_2$ and $Ni[TCNQ]_2(H_2O)_2$ occurs in a single step under voltammetric conditions [25, 32]. Formation of CuTCNQ represents a more complicated case because TCNQ is initially transformed to highly conductive and kinetically favored phase I CuTCNQ (rod or needle shaped crystals) and subsequently under conditions of cyclic voltammetry to less conductive, but thermodynamically stable, phase II CuTCNQ (rhombus-shaped crystals) [24].

Cyclic voltammetry

Figure 1 displays cyclic voltammograms obtained for the second cycle of potential at a scan rate of 20 mV s^{-1} when TCNQ crystals, adhered to a gold-coated slide electrode, are in contact with 0.1 M CuSO$_4$, CoCl$_2$, or NiCl$_2$ solution. The initial cycle of the potential is very complex [24] and is considered briefly in later discussion. The mid-point potentials E_m, where $E_m = \left(E_p^{red} + E_p^{ox} \right)\big/ 2$, and E_p^{red} and E_p^{ox} are reduction and oxidation peak potentials, for Cu–, Co–, and Ni-TCNQ systems under conditions employed in Fig. 1 are 0.11, 0.14, and 0.08 V vs Ag/AgCl, respectively. In the case of the CuTCNQ system, the reductive process presumably is associated with both the reduction of TCNQ to TCNQ$^-$ and Cu^{2+} to Cu$^+$ followed by insertion of Cu$^+$ to yield initially, phase I CuTCNQ, while the oxidative component is attributed to the overall reaction CuTCNQ $\rightarrow$ Cu^{2+} + TCNQ + 2e$^-$. On further cycling of the potential, the magnitude of the peak currents increase and formation of thermodynamically favored phase II CuTCNQ starts to be detected (Fig. 2) [24]. After five cycles, the total charge associated with the reduction and oxidation processes are almost identical, which implies that under these conditions,
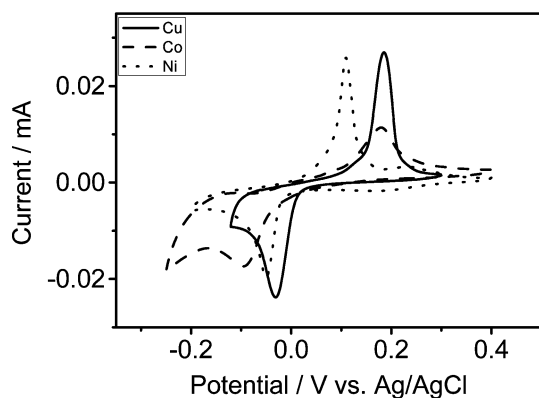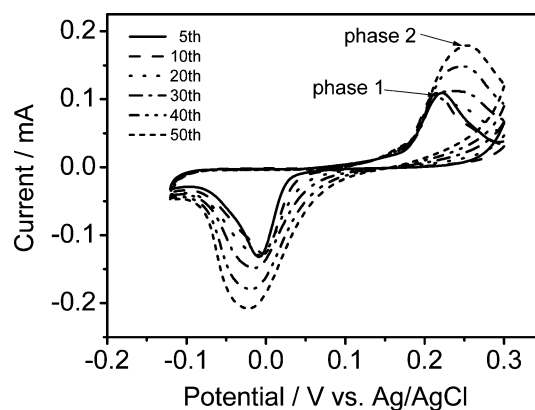

Fig. 2 Cyclic voltammograms obtained at a TCNQ-modified gold slide electrode in contact with 0.1 M CuSO$_4$ cycles 5–50 are shown over the potential range 0.3 to −0.12 V at a scan rate of 20 mV s^{-1}

approximate chemical reversibility is achieved. The oxidation peak at around 0.22 V seen in initial cycles is associated with the kinetically favored phase I, while the peak that grows at 0.26 V upon extensive cycling of the potential is derived from the thermodynamically favored phase II [24]. Cyclic voltammograms at a gold slide electrode in contact with 0.1 M CuSO$_4$, CoCl$_2$, or NiCl$_2$ solution exhibit analogous voltammetry (Fig. 1, only second cycles shown), albeit in the latter two cases, no phase changes occur upon repetitive cycling of the potential. The voltammetry on gold or ITO-coated slide electrodes (similar to gold but data not shown), as seen at conventional macro disk electrodes [32], display the characteristics of nucleation-growth mechanism for the solid–solid transformation processes.

Continuous cycling over the potential range shown in Fig. 1 is unlikely to lead to the formation of large MTCNQ crystals, as their growth will be continuously disrupted by the sequence of ingress and egress of metal ions. Controlled potential reductive electrolysis of solid TCNQ, in contact with metal ions, is therefore more likely to achieve this outcome. In a typical experiment of the latter kind, the potential used for the reductive electrolysis before in situ AFM imaging was determined from examination of cyclic voltammograms obtained at a scan rate of 20 mV s^{-1} (Fig. 1). Thus, bulk reductive electrolysis potentials for Cu, Co, Ni used in conjunction with AFM imaging were set at −0.12, −0.18, and −0.18 V, while for bulk oxidative electrolysis, the potentials chosen were 0.30, 0.30, and 0.20 V, respectively.

In situ AFM characterization of the formation of MTCNQ

CuTCNQ

Ideally, all AFM images would be obtained from the same well-shaped rhombic TCNQ crystals, to maintain all

Fig. 1 Cyclic voltammograms (second cycle of potential) at a scan rate of 20 mV s^{-1} obtained from a drop-casted TCNQ gold slide modified electrode in contact with aqueous 0.1 M CuSO$_4$ (solid line), 0.1 M CoCl$_2$ (dashed line), and 0.1 M NiCl$_2$ (dotted line) solution

parameters related to crystal dimension at constant values. However, in practice, on imaging a crystal, the AFM tip can modify the crystal surface morphology even when the tapping force is at the lowest possible level. Thus, each AFM image is derived from different, although similarly sized TCNQ crystals of about 50×50 μm^2, which represents a significant fraction of the total TCNQ crystal population. Other crystals present on the surface are generally smaller in size and less uniform.

In the case of CuTCNQ, a 20×20 μm^2 AFM image of the top surface of an approximately 50×50 μm^2 crystal was collected initially at open circuit potential. Two further images were then captured after reductive electrolysis for 5 and 10 min. Finally, images were taken after 2.5, 20.5, and 50.5 cycles over the potential range.

The AFM image in Fig. 3a reveals that pristine 50×50 μm^2 TCNQ crystals are relatively flat, with only a few nanometers of roughness detected. After 5 min of reductive electrolysis at constant potential (Fig. 3b), many small crystals appeared, with a few already developed into rod-like shapes expected for phase I CuTCNQ. After 10 min of reductive electrolysis (Fig. 3c), the majority of the crystals exhibited the rod-like shape. There is a relatively homogeneous distribution, with an average length of 2.18 ± 0.45 μm and average width of 370 ± 37 nm, an average height of 100 ± 23 nm, and an aspect ratio of about 5.9. The fact that the width is significantly larger than the height could be due to the rod-like crystals being partially buried in the TCNQ crystal. Details of AFM imaging experiments after potential

cycling experiments are as follows. After 2.5 cycles of the potential [end potential is negative (−)), tiny crystals are detected on the surface at random locations (Fig. 3d). It is interesting to compare their AFM result with information derived from cyclic voltammetry (Fig. 4). In the first 2.5 cycles of potential, the voltammetric signal changes dramatically, while the morphology as deduced from the AFM images of large crystal surfaces changes only slightly (Fig. 3d). However, voltammetric data reflects an average change associated with all crystals on the surface that include more rapidly reduced smaller crystals, while AFM images only represent a specific region on a large 50×50 μm^2 crystals. Consequently, AFM images were obtained from at least five experiments and also on five different crystals to ensure that the images shown in Fig. 4 represent typical crystal morphology.

After 20.5 cycles of the potential, Phase I CuTCNQ should be dominant, but with phase II detectable according to voltammetric data (Fig. 2). The AFM image obtained on a large crystal (Fig. 3e) is consistent with the electrochemical data. Thus, most of the crystals on the surface are rod-like, which is the characteristic morphology associated with phase I CuTCNQ [24], although several rhombus-like crystals appear in the bottom-right part of the image. After 50.5 cycles, the majority of the CuTCNQ crystals should be phase II, as deduced from cyclic voltammetric data (Fig. 2). The AFM image (Fig. 3f) supports this conclusion. Different-sized rhombus-like crystals now cover much of the surface. A mechanism for this phase change induced by
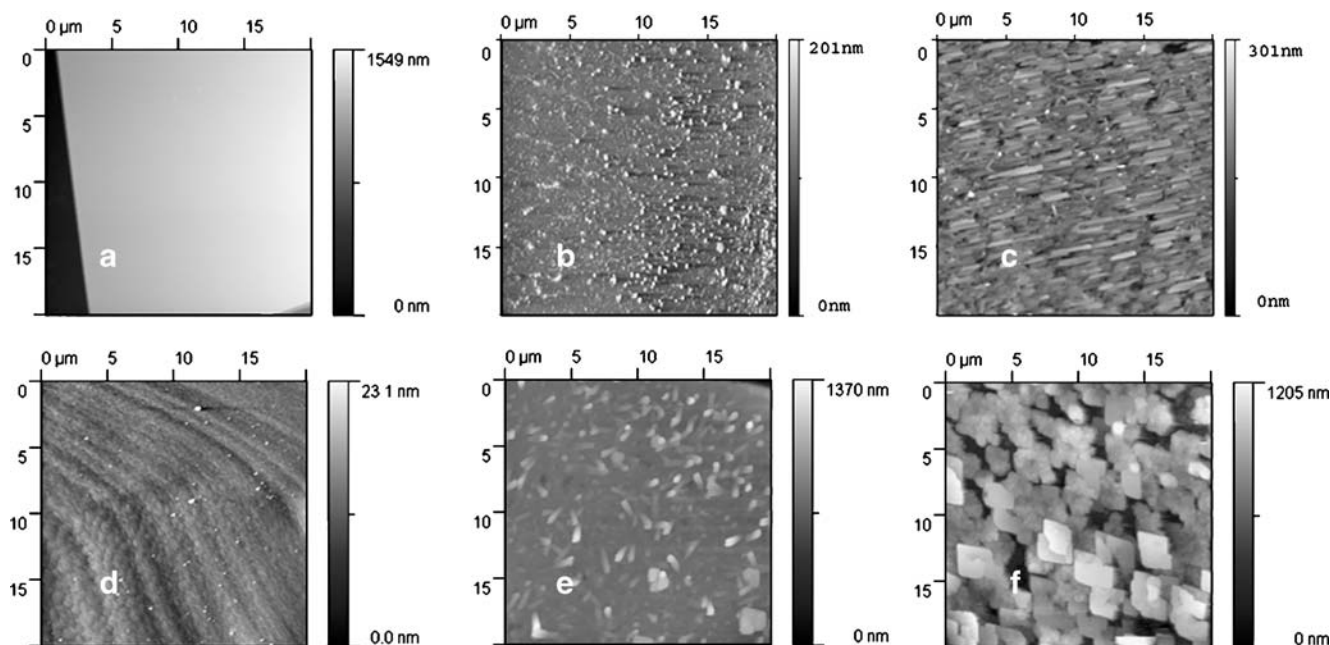

Fig. 3 AFM images, 20×20 μm^2, showing the formation of CuTCNQ from approximately 50×50 μm^2 TCNQ crystals adhered to an ITO electrode in contact with aqueous 0.1 M CuSO$_4$ solution. **a** a pristine TCNQ crystal at open circuit potential; **b** after reductive electrolysis at −0.12 V for 5 min; **c** after reductive electrolysis at −0.12 V for 10 min; **d** after 2.5 cycles of the potential; **e** after 20.5 cycles of potential; **f** after 50.5 cycles of potential. The scan size for all the images is 20 μm
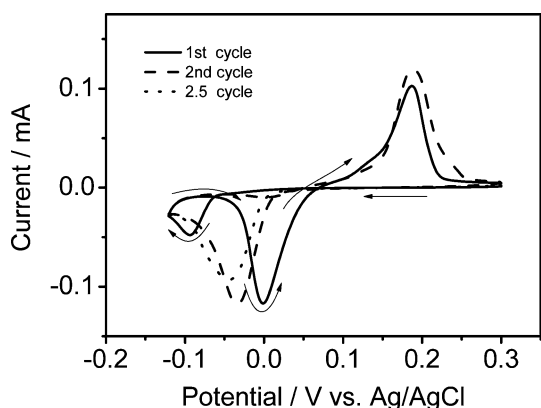
Fig. 4 Cyclic voltammogram obtained when a drop-casted TCNQ crystal modified gold slide electrode is in contact with aqueous 0.1 M $CuSO_4$ solution. The potential range is 0.3 to −0.12 V, and the scan rate is 20 mV s^{-1}. First cycle (*solid line*), second cycle (*dashed line*); 2.5 cycles (*dotted line*)

exhaustive cycling of the potential has been presented previously by Neufeld et al. [24].

To confirm the effect of the potential cycling rather than time in determining the morphology after CuTCNQ Phase I was formed, the sample was left in solution overnight, and a new AFM observation was made. No change in the AFM image was identified.

$Co[TCNQ]_2(H_2O)_2$

The procedure adopted to obtain AFM images of the TCNQ to $Co[TCNQ]_2(H_2O)_2$ transformation was the same as discussed for formation of CuTCNQ. However, in this case, it was not easy to obtain good quality images from the first few cycles of the potential. The reason for this is thought to be related to AFM imaging problems encountered from the presence of initially generated small $Co[TCNQ]_2(H_2O)_2$ rod-shaped nucleus crystals protruding outwards from the surface. Nevertheless, after reductive electrolysis for 5 min (Fig. 5a), good quality images were obtained, which revealed a predominance of evenly dispersed rod-like shaped crystals with a horizontal alignment. The size distribution of the crystals as deduced from

several experiments on $50 \times 50~\mu m^2$ TCNQ crystals was found to be relatively narrow, having a characteristic length of $1.55 \pm 0.30~\mu m$, height of 130 ± 33 nm, and width of 300 ± 28 nm, and an aspect ratio of about 5.2.

It is also informative to probe the morphology under oxidative electrolysis conditions where metal ions should be removed from the lattice. In principle, reductive electrolysis for 5 min, followed by oxidative electrolysis for 10 min should ensure that all the cobalt ions are removed. However, almost 20% of the crystals retain their rod-like structures (Fig. 5b). It is likely that the rods detected in Fig. 5b remain as $Co[TCNQ]_2(H_2O)_2$ because they have become electrochemically disconnected from the electrode surface. Even longer electrolysis times or change of the substrate from ITO to gold, still leads to detection of residual $Co[TCNQ]_2(H_2O)_2$. Thus, the $Co[TCNQ]_2(H_2O)_2$/ TCNQ process is not fully reversible under these bulk electrolysis conditions. Raman spectroscopic evidence (described later) also supports this conclusion. In contrast, if adherence of TCNQ by the method referred to as mechanical attachment is employed [25], the process seems to be essentially exhaustive in both reduction and oxidation directions, and are hence, fully reversible [25]. In the mechanical attachment method, the TCNQ crystals are fragmented into tiny crystals (typically several microns in size) before being adhered to the electrode surface, resulting in a structure that is more akin to a film rather than an array of large crystals on the surface. This thin film-like configuration enables more rapid ingress and egress of ions from the structure, and consequently, behavior is closer to exhaustive bulk electrolysis in both directions.

Ex situ SEM images obtained after reductive electrolysis of a TCNQ-modified ITO electrode in contact with 0.1 M $Co(NO_3)_2.6H_2O$ aqueous solution at −0.05 V for 10 min also revealed the formation of a $Co[TCNQ]_2(H_2O)_2$ network of nanorods (Fig. 6a). The close relationship to in situ AFM images implies that removal of the solvent environment required to obtain SEM images does not alter the morphology. SEM images therefore may be used to support AFM evidence that the overall rhombus shape of

Fig. 5 AFM images of Co $[TCNQ]_2(H_2O)_2$ crystals formed by reduction of $50 \times 50~\mu m^2$ TCNQ crystals which have been adhered to an ITO electrode in contact with aqueous 0.1 M $CoCl_2$ solution: **a** after reductive electrolysis at −0.18 V for 5 min, **b** as for (**a**) followed by oxidative electrolysis at 0.30 V for 10 min
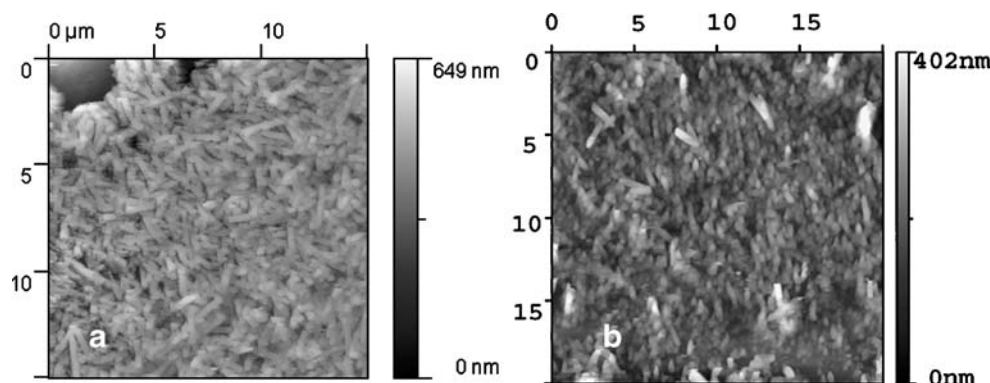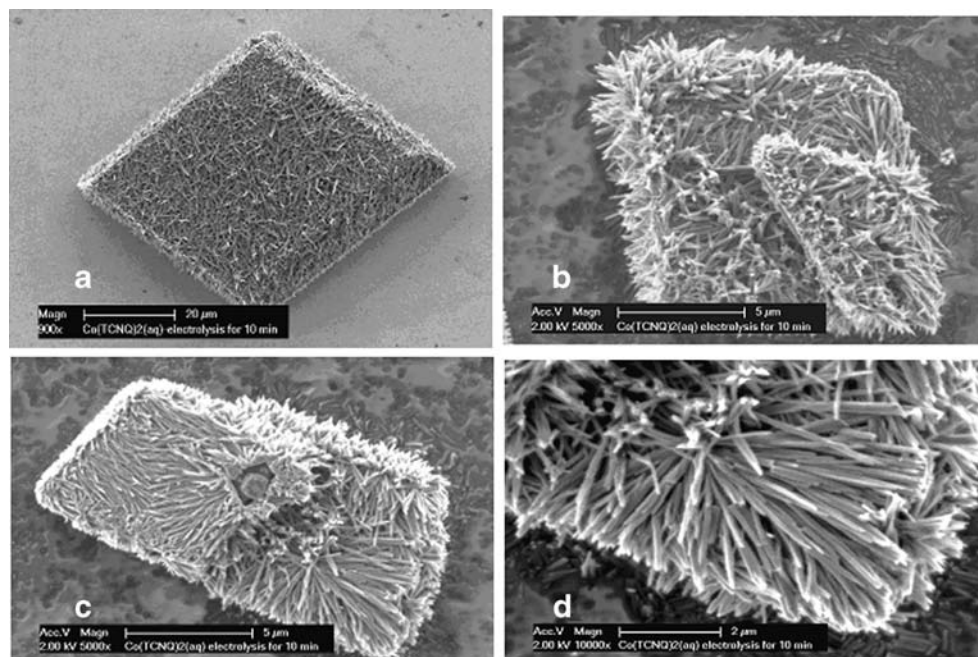
Fig. 6 a SEM image of the top face of a drop cast TCNQ crystal when Co[TCNQ]$_2$(H$_2$O)$_2$ is formed by reductive electrolysis of a TCNQ modified ITO electrode for 10 min at −0.05 V in the presence of aqueous 0.1 M Co(NO$_3$)$_2$ solution. b–d SEM images obtained of the bottom face of the crystal when Co[TCNQ]$_2$(H$_2$O)$_2$ is formed under the same conditions as for (a)

the parent TCNQ crystal structure remains intact after formation of Co[TCNQ]$_2$(H$_2$O)$_2$, and also that after extensive reduction, Co[TCNQ]$_2$(H$_2$O)$_2$ nanorods almost completely cover both the edges and top of the large parent precursor TCNQ crystal. This outcome addressed a fundamental question concerning the nature and location of the initial nucleation/growth sites associated with the solid–solid electrochemically induced TCNQ/Co[TCNQ]$_2$(H$_2$O)$_2$ transformation process. From an energetic point of view, the triple phase solid | electrode | electrolyte junction should provide the location for the initial nucleation sites [33–36]. Presumably, growth would commence from the bottom edge of the TCNQ crystal, with the fastest rate being along the edge surfaces rather than through the center of the TCNQ crystal. This "network" type nucleation-growth process would be facilitated by the semiconducting nature of Co[TCNQ]$_2$(H$_2$O)$_2$. Thus, the area of the electrode surface effectively increases as crystal growth extends.

Presumably, the rate of growth into the interior of TCNQ crystals may be restricted by Ohmic drop (iR_u, i=current, R_u=uncompensated resistance) considerations and lack of ready access to Co$^{2+}_{(aq)}$ ions.

To gain additional insight into the location of the initial nucleation and growth stage, we repeated the reductive electrolysis experiments, but now examined SEM images derived from the bottom face of the TCNQ crystal. Thus, after 10 min electrolysis in the presence of Co$^{2+}_{(aq)}$ electrolyte, the top face of the Co[TCNQ]$_2$(H$_2$O)$_2$-modified ITO electrode was pressed onto a carbon tape, and the adhered solid was removed from the ITO surface. Using this method, ex situ SEM images of the solid that had been in direct contact with the electrode surface could be obtained, i.e., the bottom face of the TCNQ crystals. Inspection of the images (Fig. 6b–d) revealed that the bases of the large rhombic-shaped TCNQ crystals have become completely covered with needle-shaped Co[TCNQ]$_2$(H$_2$O)$_2$

Fig. 7 AFM images of Ni[TCNQ]$_2$(H$_2$O)$_2$ crystals formed by reduction of 50× 50 μm^2 TCNQ crystals adhered to an ITO electrode in contact with aqueous 0.1 M NiCl$_2$ solution. a after reductive electrolysis at −0.18 V for 5 min. b image of (a) obtained at higher magnification
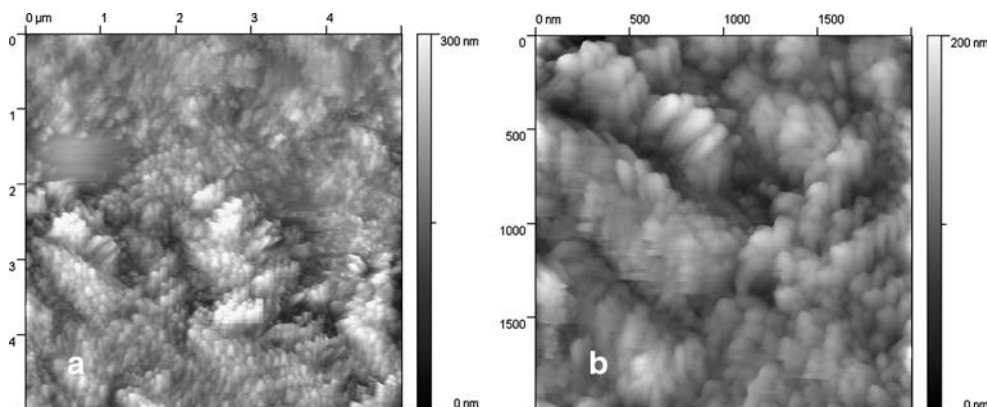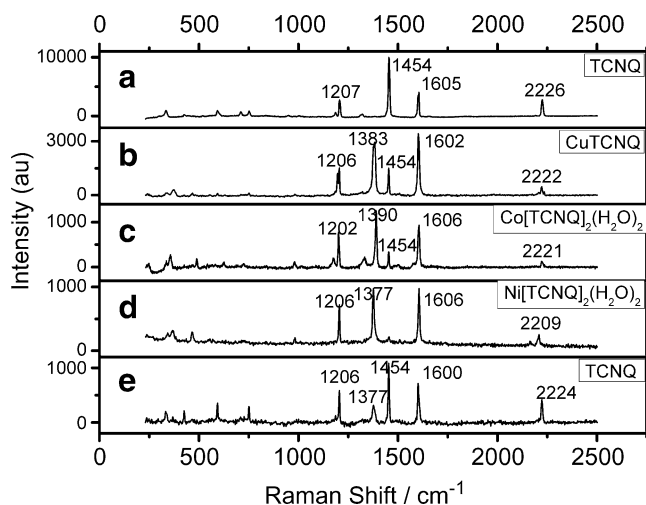
Fig. 8 Raman spectra obtained for **a** TCNQ adhered to a gold slide electrode before reductive electrolysis; **b**, **c**, and **d** MTCNQ formed by reductive electrolysis for 10 min when TCNQ is adhered to a gold slide electrode in contact with aqueous 0.1 M CuSO$_4$ (**b**), 0.1 M CoCl$_2$ (**c**), 0.1 M NiCl$_2$ (**d**); **e** Spectrum produced by oxidative electrolysis of Ni[TCNQ]$_2$(H$_2$O)$_2$ formed in (**d**)

crystals having a length of ∼2 μm and a width of ∼100–200 nm. This observation supports the hypothesis that the initial nucleation sites occur at locations where direct contact between electrode surface, electrolyte and solid TCNQ occurs. Presumably, ingress of Co$^{2+}_{(aq)}$ may occur below the bottom face of the TCNQ surface because neither the TCNQ solid nor electrode surface are fully flat, thereby allowing aqueous electrolyte to penetrate between these two regions.

Ni[TCNQ]$_2$(H$_2$O)$_2$

Ni[TCNQ]$_2$(H$_2$O)$_2$ is formed by solid–solid conversion of TCNQ (Eq. 3) in an analogous manner to that for Co[TCNQ]$_2$(H$_2$O)$_2$. Ni[TCNQ]$_2$(H$_2$O)$_2$ also exists in only one phase as rod-like crystals. However, Ni[TCNQ]$_2$(H$_2$O)$_2$ forms much smaller crystals than Co[TCNQ]$_2$(H$_2$O)$_2$ with a preferential orientation into the bulk solution. Fig. 7 contains AFM images after reductive electrolysis for 5 min at different magnifications. Typically, the numerous tiny Ni[TCNQ]$_2$(H$_2$O)$_2$ rods protrude from the substrate. The typical size detected under conditions of Fig. 7 is 300 nm in length and 80 nm in width. In contrast, the dominant feature in images of Co[TCNQ]$_2$(H$_2$O)$_2$ were horizontally oriented and were much longer rods of 1.5 μm in length and 300 nm wide.

Raman spectroscopic characterization of solid–solid electrochemical conversion

Raman spectra [37–40] obtained in the ex situ mode allow a ready distinction between TCNQ and [TCNQ]$^{.-}$-containing

compounds, and hence, allow the course of reduction and oxidation on the surface of 50×50 μm^2 crystals to be monitored. Thus, upon solid–solid transformation of TCNQ into MTCNQ, it is expected that the frequency of the 1,454 cm^{-1} C–CN stretch in TCNQ (Fig. 8a) would shift to about 1,380 cm^{-1} if [TCNQ]$^{.-}$ is formed. In addition, the 2,225 cm^{-1} C≡N stretching band (Fig. 8a) in TCNQ shoud shift to a lower wavelength upon reduction, and the total Raman intensity should drop significantly due to the higher absorbance of MTCNQ and concomitant decrease in the scattering volume [37–40].

In the case of electrochemical formation of CuTCNQ and Co[TCNQ]$_2$(H$_2$O)$_2$ (see Fig. 8b,c) by reductive electrolysis of TCNQ for 10 min, ex situ detection of Raman bands at 1,383 and 1,390 cm^{-1}, respectively is indicative of [TCNQ]$^{.-}$ formation. However, retention of the band at 1,454 cm^{-1} indicates that residual TCNQ also is still present. The TCNQ band at 2,226 cm^{-1} shifts only slightly to around 2,220 cm^{-1}. Thus, according to Raman spectra evidence, the majority of the 50×50 μm^2 TCNQ surface has been changed to M$^+$[TCNQ]$^{.-}$, but some TCNQ remains. The laser detection spot used in Raman spectroscopy can penetrate to a depth of several microns. Thus, residual TCNQ, which is detected, may not lie on the surface. For Ni[TCNQ]$_2$(H$_2$O)$_2$, the transformation is quantitative with respect to Raman spectroscopic evidence (Fig. 8d). In this case, the 1,454 cm^{-1} band fully disappeared upon reduction, while the 2,225 cm^{-1} band shifted to 2,209 cm^{-1}. It is plausible that this is associated with the much smaller Ni[TCNQ]$_2$(H$_2$O)$_2$ crystal size and their prevailing direction into the solution phase. Ex situ Raman spectra (Fig. 8e) shows that after applying a potential required to transform Ni[TCNQ]$_2$(H$_2$O)$_2$ back to TCNQ, the 2,209 cm^{-1} resonance reverts back to 2,224 cm^{-1}, as expected if MTCNQ is transformed back to TCNQ with egress of the Ni^{2+} ions. However, the 1,377-cm^{-1} resonance remains detectable, although significantly lower in intensity. A similar situation prevails for the other TCNQ/MTCNQ processes. These data, in agreement with conclusions reached by in situ AFM morphology data, suggest that while most of the solid MTCNQ can be electrochemically converted back to TCNQ, residual amounts remain even when the potential is held at sufficiently positive potential for long periods of time.

Conclusions

In situ AFM images of the electrochemically induced solid–solid TCNQ/MTCNQ transformation provides insights into the nucleation growth process that allow redox interconversion of the two solids. By controlling the time of reductive electrolysis, nearly mono-dispersed rod-like

MTCNQ can be obtained on the face and side of original relatively flat rhombic-shaped 50×50 μm^2 TCNQ crystals. Ex situ SEM imaging of the underside of the crystals also reveals that the nucleation-growth process takes place where the electrode is in direct contact with TCNQ and presumably also with electrolyte. For CuTCNQ, the morphology change connected with phase I to phase II transformation that occurs under conditions of cyclic voltammetry also can be detected. During the process of crystal solid–solid state transformation, the initial nucleation site is likely to be the solid | electrode | electrolyte junction, with growth favored along the surface of the crystal. Significant differences in morphology are associated with each TCNQ/MTCNQ transformation. Raman spectra and AFM images suggest that 100% interconversion is not always achieved even after extensive electrolysis of large 50×50 μm^2-sized TCNQ crystals.

References

1. Acker DS et al (1960) J Am Chem Soc 82:6408–6409
2. Krysinski P, Tien HT (1988) Bioelectrochem and Bioenerg 19:227–233
3. Freund MS, Brajtertoth A, Ward MD (1990) J Electroanal Chem 289:127–141
4. Nakajima K, Kageshima M, Ara N, Yoshimura M, Kawazu A (1993) Appl Phys Lett 62:1892–1894
5. Bond AM, Fletcher S, Marken F, Shaw SJ, Symons PG (1996) J Chem Soc-Faraday Trans 92:3925–3933
6. Chambers JQ, Scaboo K, Evans CD (1996) J Electrochem Soc 143:3039–3045
7. Bartlett PN, Tong XQ (1997) J Phys Chem B 101:8540–8549
8. Bond AM, Fiedler DA (1997) J Electrochem Soc 144:1566–1574
9. Bond AM, Fletcher S, Symons PG (1998) Analyst 123:1891–1904
10. Oyama M et al (1998) J Phys Chem B 102:6588–6595
11. Bellec V et al (2001) Electrochem Comm 3:483–488
12. Fraxedas J, Langer J, Diez I, Sanz F (2006) J Low Temp Phys 142:121–126
13. Gomez L, Rodriguez-Amaro R (2006) Langmuir 22:7431–7436
14. Liu YL et al (2006) J Am Chem Soc 128:12917–12922
15. O'Mullane AP, Neufeld AK, Bond AM (2005) Anal Chem 77:5447–5452
16. Neufeld AK, O'Mullane AP, Bond AM (2005) J Am Chem Soc 127:13846–13853
17. Harris AR, Neufeld AK, O'Mullane AP, Bond AM, Morrison RJS (2005) J Electrochem Soc 152:C577–C583
18. Cao GY et al (2005) Micron 36:267–270
19. Zhang Q, Kong LZ, Zhang QJ, Wang WJ, Hua ZY (2004) Solid State Commun 130:799–802
20. Liu SG, Liu YQ, Wu PJ, Zhu DB (1996) Chem Mater 8:2779–2787
21. Heintz RA et al (1999) Inorg Chem 38:144–156
22. Liu YL et al (2005) Adv Mater 17:2953–2957
23. Potember RS, Poehler TO, Cowan DO, Bloch AN (1981) Bull Amer Phys Soc 26:309
24. Neufeld AK, Madsen I, Bond AM, Hogan CF (2003) Chem Mater 15:3573–3585
25. Nafady A, O'Mullane AP, Bond AM, Neufeld AK (2006) Chem Mater 18:4375–4384
26. Hoagland JJ, Wang XD, Hipps KW (1993) Chem Mater 5:54–60
27. Wan LJ, Itaya K (2001) Chin Sci Bull 46:377–380
28. Magonov SN, Bar G, Cantow HJ, Ren J, Whangbo MH (1994) Synth Met 62:159–167
29. Higo M, Lu X, Mazur U, Hipps KW (2001) Thin Solid Films 384:90–101
30. Suarez MF, Bond AM, Compton RG (1999) J Solid State Electrochem 4:24–33
31. Bond AM (2002) Broadening electrochemical horizons: principles and illustration of voltammetric and related techniques, Chapter 5. Oxford University Press, Oxford
32. Nafady A, Bond AM (2007) Inorg Chem 46:4128–4137
33. Bak E, Donten M, Stojek Z, Scholz F (2007) Electrochem Comm 9:386–392
34. Deng Y et al (2005) J Phys Chem B 109:14043–14051
35. Hasse U, Scholz F (2001) Electrochem Comm 3:429–434
36. Hermes M, Scholz F (2000) Electrochem Comm 2:845–850
37. Suchanski MR, Vanduyne RP (1976) J Am Chem Soc 98:250–252
38. Hu ZP et al (1995) J Mol Struct 356:163–168
39. Makowski M, Pawlikowski MT (2006) Int J Quantum Chem 106:1736–1748
40. Gucciardi PG, Trusso S, Vasi C, Patane S, Allegrini M (2002) Phys Chem Chem Phys 4:2747–2753